A&A 459, 693–701 (2006)
DOI: 10.1051/0004-6361:20054632

Astronomy & Astrophysics

XMM-Newton and *Chandra* measurements of the AGN intrinsic absorption: dependence on luminosity and redshift⋆

A. Akylas[1], I. Georgantopoulos[1], A. Georgakakis[2], S. Kitsionas[3], and E. Hatziminaoglou[4]

[1] Institute of Astronomy & Astrophysics, National Observatory of Athens, I. Metaxa & B. Pavlou, Penteli, 15236, Athens, Greece
e-mail: th@astro.noa.gr
[2] Physics Department, Imperial College of Science Technology and Medicine, Blackett Laboratory, Prince Consort Rd, 2BZ SW7, London, UK
[3] Astrophysikalisches Institut Potsdam, An der Sternwarte 16, 14482, Potsdam, Germany
[4] Institute de Astrofisica de Canarias, C/via Lactea s/n, 38200 La Laguna, Spain

Received 2 December 2005 / Accepted 8 June 2006

ABSTRACT

We combine bright *XMM-Newton* data with the *Chandra* Deep Field South observations to explore the behavior of the intrinsic AGN absorption, as a function of redshift and luminosity. Our sample consists of 359 sources selected in the hard 2–8 keV band, spanning the flux range 6×10^{-16}–3×10^{-13} erg cm^{-2} s^{-1} with a high rate of spectroscopic or photometric redshift completeness (100 and 85 per cent respectively for the *Chandra* and *XMM-Newton* data). We derive the column density values using X-ray spectral fits. We find that the fraction of obscured AGN falls with increasing luminosity in agreement with previous findings. The fraction of obscured AGN shows an apparent increase at high redshifts ($z > 2$). Simulations show that this effect can most probably be attributed to the fact that at high redshifts the column densities are overestimated.

Key words. surveys – X-rays: galaxies – X-rays: general

1. Introduction

Ultra-deep surveys with *Chandra* have resolved the bulk of the X-ray background at hard energies (2–10 keV), shedding light on the nature of the AGN population at faint fluxes ($f_X(2-8\ \mathrm{keV}) \sim 1.4 \times 10^{-16}$ erg cm^{-2} s^{-1}; Mushotzky et al. 2000; Giacconi et al. 2002; Alexander et al. 2003). These surveys have revealed luminous unobscured QSOs, but also, more importantly, large numbers of obscured AGN ($N_H > 10^{22}$ cm^{-2}). The fraction of absorbed sources rises steeply with decreasing flux (e.g., Alexander et al. 2003) dominating the X-ray population at the flux limit of the 2 Ms *Chandra* Deep Field North (CDF-N) survey (e.g., Perola et al. 2004). At the first approximation, this trend is in qualitative agreement with the predictions of the X-ray background (XRB) population synthesis models (e.g., Comastri et al. 1995; Gilli et al. 2001). A more detailed quantitative comparison, however, reveals a number of inconsistencies. For example, the models above also predict large numbers of luminous ($L_X > 10^{44}$ erg s^{-1}) heavily obscured ($N_H > 10^{22}$ cm^{-2}) type-II QSOs, although only a handful of such objects have been identified to date, despite painstaking efforts (e.g., Barger et al. 2003; Fiore et al. 2003; Szokoly et al. 2004). Parallel to the *Chandra* deep fields, surveys with the *XMM-Newton*, probing on average brighter fluxes, also provide a wealth of complementary information on the nature and the evolution of the AGN population. These brighter surveys also show a clear scarcity of obscured AGN relative to the model expectations (e.g., Piconcelli et al. 2002; Georgantopoulos et al. 2004; Perola et al. 2004).

Although the source of the inconsistency between observations and model predictions remains unclear, two main scenarios are put forward to reconcile the problem. The first argues that observational biases are affecting our conclusions, while the second proposes major revision of the basic assumptions of the XRB models. In the former case, it is proposed that obscured AGN are present in current surveys, but lie in poorly explored regions of the parameter space. For example, a large fraction of X-ray sources, particularly in the *Chandra* deep fields (about 30%, Alexander et al. 2003) are optically faint ($R > 24.5$ mag), and therefore, hard to study in detail. Treister et al. (2004) argue that it is precisely this poorly explored population that comprises a large fraction of obscured AGN at high redshift. This is because, although the energetic X-ray photons of these systems can penetrate the large obscuring columns of gas and dust, the rest-frame UV/optical light is heavily extincted, resulting in faint observed optical magnitudes. Consequently the type-II AGN are difficult spectroscopic targets, even with 10-m class telescopes, and their intrinsic properties (including their N_H) remain ill constrained.

In the case of the model revision scenario, one of the key input parameters to the XRB models is the intrinsic column density (N_H) distribution of AGN. This is assumed to be that of Seyfert galaxies (i.e., low-luminosity AGN) measured from the local Universe (Risaliti et al. 1999). It is possible that the luminous AGN identified in deeper surveys do not follow the same column density distribution, leading to the failure of the population synthesis models. Indeed, by combining sources with redshift information from the CDF-N and brighter *ASCA* surveys, Ueda et al. (2003) find that the fraction of obscured AGN

⋆ Table 2 and Appendix A are only available in electronic form at http://www.aanda.org

Table 1. The 28 archival *XMM-Newton* pointings used in this study.

RA (J2000)	Dec (J2000)	Filter FILTER	$N_{\rm Hgal}$ ($\times 10^{20}$ cm^{-2})	PN exp. time (s)	MOS exp. time (s)	Field name
$23^{\rm h}54^{\rm m}09.0^{\rm s}$	$-10°24'00''$	MEDIUM	2.91	13 600	19 100	ABELL 2670
$23^{\rm h}37^{\rm m}40.0^{\rm s}$	$+00°16'33''$	THIN	3.82	8200	13 300	RXCJ 2337.6+0016
$17^{\rm h}01^{\rm m}23.0^{\rm s}$	$+64°14'08''$	MEDIUM	2.65	2300	3900	RXJ 1701.3
$15^{\rm h}43^{\rm m}59.0^{\rm s}$	$+53°59'04''$	THIN	1.27	14 200	19 200	SBS 1542+541
$13^{\rm h}49^{\rm m}15.0^{\rm s}$	$+60°11'26''$	THIN	1.80	14 100	18 100	NGC 5322
$13^{\rm h}04^{\rm m}12.0^{\rm s}$	$+67°30'25''$	THIN	1.80	14 600	17 100	ABELL 1674
$12^{\rm h}45^{\rm m}09.0^{\rm s}$	$+00°27'38''$	MEDIUM	1.73	46 300	55 500	NGC 4666
$12^{\rm h}31^{\rm m}32.0^{\rm s}$	$+64°14'21''$	THIN	1.98	26 100	30 100	MS 1229.2+6430
$09^{\rm h}35^{\rm m}51.0^{\rm s}$	$+61°21'11''$	THIN	2.70	20 400	33 900	UGC 5051
$09^{\rm h}34^{\rm m}02.0^{\rm s}$	$+55°14'20''$	THIN	1.98	23 500	28 500	IZW 18
$09^{\rm h}17^{\rm m}53.0^{\rm s}$	$+51°43'38''$	MEDIUM	1.44	15 900	13 600	ABELL 773
$08^{\rm h}31^{\rm m}41.0^{\rm s}$	$+52°45'18''$	MEDIUM	3.83	66 800	73 300	APM 08279+5255
$03^{\rm h}57^{\rm m}22.0^{\rm s}$	$+01°10'56''$	THIN	13.20	19 100	21 400	HAWAII 167
$03^{\rm h}38^{\rm m}29.0^{\rm s}$	$+00°21'56''$	THIN	8.15	8900	6700	SDSS 033829.31+00215
$03^{\rm h}02^{\rm m}39.0^{\rm s}$	$+00°07'40''$	THIN	7.16	38 100	46 900	CFRS 3H
$02^{\rm h}56^{\rm m}33.0^{\rm s}$	$+00°06'12''$	THIN	6.50	–	11 600	RX J0256.5+000
$02^{\rm h}41^{\rm m}05.0^{\rm s}$	$-08°15'21''$	MEDIUM	3.07	12 300	15 600	NGC 1052
$01^{\rm h}59^{\rm m}50.0^{\rm s}$	$+00°23'41''$	MEDIUM	2.65	3800	–	MRK 1014
$01^{\rm h}52^{\rm m}42.0^{\rm s}$	$+01°00'43''$	MEDIUM	2.80	5800	17 200	ABELL 267
$00^{\rm h}43^{\rm m}20.0^{\rm s}$	$-00°51'15''$	MEDIUM	2.33	15 700	–	UM 269
$13^{\rm h}41^{\rm m}24.0^{\rm s}$	$+00°24'00''$	THIN	2.00	5779	9974	F864-1
$13^{\rm h}43^{\rm m}00.0^{\rm s}$	$+00°24'00''$	THIN	2.00	2958	6586	F864-2
$13^{\rm h}44^{\rm m}36.0^{\rm s}$	$+00°24'00''$	THIN	2.00	2187	7727	F864-3
$13^{\rm h}43^{\rm m}00.0^{\rm s}$	$+00°00'00''$	THIN	2.00	1693	4447	F864-5
$13^{\rm h}44^{\rm m}36.0^{\rm s}$	$+00°00'00''$	THIN	2.00	2766	6493	F864-6
$13^{\rm h}\ 41^{\rm m}24.0^{\rm s}$	$-00°24'00''$	THIN	2.00	3459	7139	F864-7
$13^{\rm h}43^{\rm m}24.0^{\rm s}$	$-00°24'00''$	THIN	2.00	2109	7276	F864-8
$13^{\rm h}44^{\rm m}36.0^{\rm s}$	$-00°24'00''$	THIN	2.00	4545	8330	F864-9

diminishes with increasing luminosity. The physical interpretation of this model could be that the highly luminous AGN blow away the obscuring screen or they photoionize the gas around them. More recently, La Franca et al. (2005) estimated the fraction of absorbed AGN as a function of luminosity combining data from the CDF-N and Chandra Deep Field South (CDF-S) surveys as well as bright *XMM-Newton* data. They also suggest a decrease of the obscured AGN fraction (hereafter F) with luminosity, as well as a possible increase with redshift, in contrast to the standard model assumption that F is independent of $L_{\rm X}$ and z. Such studies are obviously important for furthering our understanding of the AGN unification models, and moreover, they are crucial for the construction of X-ray background population synthesis models.

In this paper, we attempt to further investigate the intrinsic absorption in AGN, using a large X-ray sample from *XMM-Newton* and *Chandra* with X-ray spectroscopic information. In particular, we combine the CDF-S observations (162 sources, *all* with redshift information, from Szokoly et al. 2004 and Zheng et al. 2004), with *XMM-Newton* data at brighter fluxes ($>3 \times 10^{-14}$ erg cm^{-2} s^{-1}) from the HELLAS2XMM survey of Perola et al. (2004) (44 sources), and our own *XMM-Newton* survey, which overlaps with the Sloan Digital Sky Survey (SDSS) (153 sources). The advantages of our approach are the following:

- We have derived X-ray spectra for all the X-ray sources in our sample, trying to avoid the uncertainties that can be introduced by a simple X-ray color.
- We estimate the fraction of obscured AGN using the $1/V_m$ method. In this way, we properly take into account the "accessible" volume of each source, i.e., the fact that many obscured sources are not detected at a given flux limit.
- We use the CDF-S, instead of the CDF-N, as the former has photometric or spectroscopic redshifts for all the sources. This means that there are no missing type-II AGN at high redshifts, which would introduce a spurious correlation between obscured fraction and luminosity.

Throughout this paper we adopt $H_0 = 70$ km s^{-1} Mpc^{-1}, $\Omega_{\rm m} = 0.3$, and $\Lambda = 0.7$.

2. The X-ray data

2.1. The XMM-Newton data

The *XMM-Newton* X-ray data come from 28 public fields selected to overlap with the second data release of the SDSS (DR2; Stoughton et al. 2002) and cover a total area of ∼5 sq. degrees. Eight of these fields comprise the North *XMM-Newton*/2dF survey (for details see Georgakakis et al. 2003; Georgantopoulos et al. 2004). For the fields observed more than once with *XMM-Newton*, we use the deeper of the multiple observations. The observational characteristics of the 28 *XMM-Newton* fields used here, obtained from Georgantopoulos & Georgakakis (2005), are listed in Table 1.

The X-ray data have been analyzed using the Scientific Analysis Software (SAS v6.0). The pipeline event files, produced by the *XMM-Newton* Science Center, were screened for high particle background periods by rejecting time intervals with 0.5–10 keV count rates higher than 25 and 15 cts/s for the PN and the two MOS cameras, respectively. The PN and MOS good time intervals are listed in Table 1. The differences between

the PN and the MOS exposure times are due to varying start and end times of the individual observations. We consider the events corresponding to patterns 0–4 for PN and 0–12 for the MOS instrument.

To increase the signal-to-noise (S/N) ratio and to reach fainter fluxes, we have merged the MOS and the PN data into a single event file using the *MERGE* task of SAS. The X-ray images have been extracted in the 2–8 keV (hard) energy band, for both the merged and the individual event files. We use the more sensitive (higher S/N ratio) merged image for source extraction and flux estimation, while the individual PN and MOS images are used to extract the spectral files. The source detection has been performed using the *EWAVELET* task of SAS with a detection threshold of 6σ. The choice of the threshold minimizes the number of spurious sources in the final catalogue without reducing the number of real detections. All the detected sources were carefully inspected one by one to exclude spurious detections associated with CCD gaps, hot pixels, or sources lying close to the edge of the detector's field of view. We also exclude the target source of each *XMM-Newton* and seven sources that appear extended on the *XMM-Newton* EPIC images and that are clearly associated with diffuse cluster emission from the final catalogue. We estimate the observed flux of each source in a 18 arcsec aperture, adopting a power-law energy distribution model with $\Gamma = 1.8$. The final X-ray catalogue comprises a total of 507 sources detected in the 2–8 keV merged (PN+MOS) images with a 6σ, 2–8 keV flux limit of 5×10^{-15} erg cm^{-2} s^{-1} (see Georgakakis et al. 2006a). For the purpose of this study, we consider only the brighter hard X-ray sources with a 2–8 keV flux $f_X(2\text{–}8) > 3 \times 10^{-14}$ erg cm^{-2} s^{-1} (169 sources). This is to ensure sufficient photon statistics to perform X-ray spectral analysis and to minimize the number of objects without optical identifications. The background subtracted photon count distribution of these sources is plotted in Fig. 1.

2.2. The CDF-S data

The CDF-S X-ray data are obtained from Giacconi et al. (2002). The data from these observations include 247 hard (2–10 keV) X-ray selected sources with complete spectroscopic or photometric redshift (Szokoly et al. 2004; Zheng et al. 2004). For one source (#261), there is no redshift information and hence it is excluded from our analysis.

These data expand the 2–8 keV flux coverage of our *XMM-Newton* data down to $\sim 6 \times 10^{-16}$ erg cm^{-2} s^{-1}. To increase the photon statistics, we consider only the sources that lie within the central CDF-S region, and therefore overlap with all 11 Chandra pointings. This reduces the number of the sources to 188. The vast majority of the sources (179) contain more than 50 net counts, sufficient for spectral analysis. Furthermore, we exclude 26 sources identified as normal galaxy candidates by Norman et al. (2004). Therefore, our final CDF-S AGN sample comprises 162 sources with spectroscopic (75 sources) or photometric (87 sources) redshift information. The background subtracted photon count distribution of these sources is plotted in Fig. 1.

3. The sample

We use the SDSS DR2 catalogue to optically identify the hard X-ray detected sources using the method of Downes et al. (1986; for a detailed description of the procedure followed, see Georgakakis et al. 2004) to calculate the probability, P, that a given candidate is a spurious identification. Here we apply

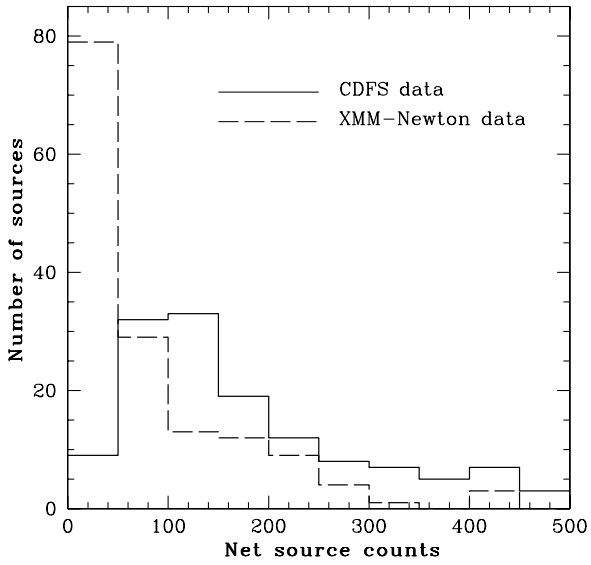

Fig. 1. The background subtracted photon count distribution for our *XMM-Newton*/SDSS data (dashed histogram) and the CDF-S survey (solid histogram).

an upper limit in the search radius, $r < 7$ arcsec, and a cutoff on the probability, $P < 0.05$, to limit the optical identification to those candidates that are least likely to be spurious alignments. The cross-correlation reveals 143 coincidences. 26 sources have no optical counterpart in the SDSS limit ($r < 22.5$ mag), giving an 85 per cent completeness for our *XMM-Newton* sample. From the data above we further exclude all the sources with extended optical morphology and blue colors, i.e., $g - r < 0.5$ mag, since the estimation of the photometric redshifts for these population is inaccurate, as we discuss below. After this selection, our catalogue comprises in total 157 hard X-ray sources. In particular, there are 45 sources with spectroscopic information, 86 with only photometric observations, and 26 optically faint sources ($r > 22.5$ mag).

For the 86 sources with photometric information available, we estimate photometric redshifts using the method described by Kitsionas et al. (2005). These authors have applied the photometric redshift estimation technique of Hatziminaoglou et al. (2000) on X-ray selected *XMM-Newton* samples, also using 5-band photometry from the SDSS. The method is based on the standard χ^2 minimization, using a combination of QSO stellar and galaxy Spectral Energy Distribution (SED) templates for the redshift estimation. In particular, the method uses the three QSO templates of Hatziminaoglou et al. (2000) produced by varying the optical power-law spectral index of simulated QSO spectra that include a variety of broad emission lines between 0 and 1. It also uses four different galaxy templates (E/S0, Sbc, Scd, Im) from Coleman et al. (1980).

Following the procedure in Kitsionas et al. (2005), we have divided the sources in our photometric sample into point-like and extended sources according to their SDSS optical morphology. We have estimated photometric redshifts, using the QSO templates for the point-like objects and the galaxy templates for the extended sources. As explained above, we have excluded extended objects with blue colors ($g - r < 0.5$), since Kitsionas et al. (2005) have shown that the photometric redshift estimations for such objects are unreliable using template fitting techniques with the existing QSO/galaxy templates, or even linear combinations of the two. Moreover, point-like sources with X-ray-to-optical flux ratio $\mathrm{Log}\,(f_X/f_{opt}) < -1$ (i.e., in the region

occupied mostly by Galactic stars; Stocke et al. 1991) are fitted with both QSO and stellar templates. Kitsionas et al. (2005) have demonstrated that this method is very efficient in identifying Galactic stars. In our sample, there are in total 4 Log $(f_X/f_{opt}) < -1$ point-like sources that are best fitted by stellar templates. These sources are excluded from our final catalogue.

Given the fact that our sample is similar in nature to the sample discussed by Kitsionas et al. (2005), we adopt the same probabilities for obtaining reliable photometric redshifts. In particular, we assume that photometric redshift estimates for QSOs in our photometric sample have ∼70% probability of being within 0.3 from the source's real redshift, whereas for red extended objects, the probability of photometric redshift estimates being within 0.15 from the source's real redshift is increased to ∼75%. Our final sample, hereafter the *XMM-Newton*/SDSS sample, comprises 26 sources without optical counterpart 45 sources spectroscopically classified, based on either SDSS or NASA Extragalactic Database (NED) classification, as QSOs, and 82 sources with photometric observations most probably associated with an AGN. In the case of the optically unidentified objects, we assume a mean redshift of 1.5 to estimate the source luminosity and the column density. Although this is clearly an arbitrary assumption, the fact that SDSS did not detect these sources suggests that their redshift is likely higher than 1. Indeed, galaxies with, e.g., Mr = −21, should be detected up to a redshift of 0.7 at the SDSS magnitude limit of $r = 22.5$. Moreover, the vast majority of these optically faint sources (22 out of 26) present $\log(f_X/f_{opt}) > 1$. Previous work in both deep *Chandra* and shallower *XMM-Newton* surveys (i.e., Alexander et al. 2002; Fiore et al. 2003) has shown that a considerable fraction of these sources are type-II QSOs.

To increase our statistics, we have included the data from the HELLAS2XMM survey (Perola et al. 2004) in our *XMM-Newton*/SDSS sample. There are 44 optically identified, hard X-ray selected QSOs in the 2–8 keV flux limit of 3×10^{-14} erg cm^{-2} s^{-1}. The conversion of their 2–10 keV intrinsic flux to our 2–8 keV band was made using an average photon index of 1.8.

In Fig. 2 we plot the redshift distribution for the two datasets. Hereafter, we consider these combined observations as the *XMM-Newton* sample. The final *XMM-Newton* catalogue comprises 197 sources, of which 171 have photometric or spectroscopic information and 26 are optically unidentified sources to the flux limit of the SDSS survey.

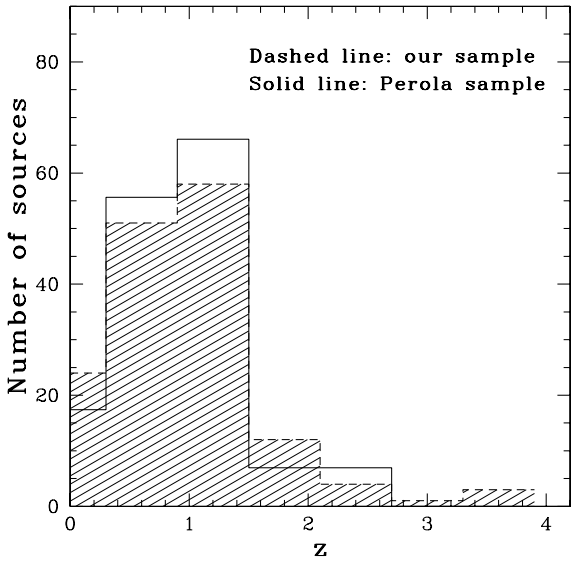

Fig. 2. The redshift distribution of our *XMM-Newton*/SDSS survey sample comprising 153 sources (shaded histogram), including the 26 optically unidentified sources, arbitrarily placed in the 1.0–1.5 redshift bin (see text). We also plot the redshift distribution of the 44 sources from the HELLAS2XMM survey (Perola et al. 2004, open histogram), normalized to our data.

4. The X-ray spectral analysis

4.1. XMM-Newton/SDSS spectral analysis

We explore the X-ray properties of the *XMM-Newton*/SDSS sample using the *XSPEC* v11.2 package to perform X-ray spectral fittings. For the sources with adequate count statistics (net source counts >100), we use the χ^2 statistic technique. The data are grouped to give a minimum of 15 counts per bin to ensure that Gaussian statistics apply. We adopt an absorbed power-law model and attempt to constrain the intrinsic absorption column density N_H (i.e., having subtracted the Galactic absorption) and the power-law photon index Γ.

For the sources with limited photon statistics (net counts <100), we use the C-statistic technique (Cash 1979) specifically developed to extract spectral information from data with a low signal-to-noise ratio. In this case, the data are grouped to give a minimum of 1 count per bin to avoid zero count bins. We try to constrain the intrinsic column densities using an absorbed power-law model with Γ fixed to 1.8.

In both cases, the spectral fittings are performed in the 0.3–8 keV energy band where the sensitivity of the *XMM-Newton* detectors is the highest. The estimated errors correspond to the 90 per cent confidence level. In Table 2 we present the spectral fitting results for the 153 sources comprising our final *XMM-Newton*/SDSS dataset. The spectral results for the 44 HELLAS2XMM survey sources have been obtained from Perola et al. (2004) and are not presented here. In Cols. 2 and 3 we list the source coordinates. In Col. 4, we give the best-fit power-law photon index (when fixed to 1.8, spectral fittings are performed using C-statistic). In Col. 5 we present the best-fit observed column density (uncorrected for redshift and Galactic absorption), and in Col. 6 the intrinsic 2–8 keV X-ray flux. Column 7 lists the source redshift, and Col. 8 the value of the Galactic absorption in the direction of the pointing. In Col. 9, we present the intrinsic column density (i.e., corrected for redshift and Galactic absorption), and in Col. 10, the intrinsic hard (2–8 keV) X-ray luminosity, using the K-correction appropriate for the best-fit value of Γ. In the last column we have included an identification key in to distinguish between data with spectroscopic observations (id = 1), photometric observations (id = 2), or without optical identification (id = 3).

The calculation of the intrinsic column density is based on the formula $N_{Hintr} = (N_{Hobs} - N_{Hgal}) \cdot (1+z)^{2.65}$. We have assumed a minimum value for the intrinsic column density, $N_{H_{intr}}^{min} = (N_{H_{obs}}^{min}) \cdot (1+z)^{2.65}$, where $N_{H_{obs}}^{min} = 10^{20}$ cm^{-2} is approximately the minimum column density that can be detected in the observed 0.3–8 keV energy range by the *XMM-Newton* EPIC PN or MOS CCDs. Also, in the cases where the spectral fitting analysis indicates a very flat spectrum (i.e., Γ < 1.0, see the sources #50 and #85 in Table 2), we assume that these sources are Compton thick and the N_H value is arbitrarily set to 5×10^{24} cm^{-2}.

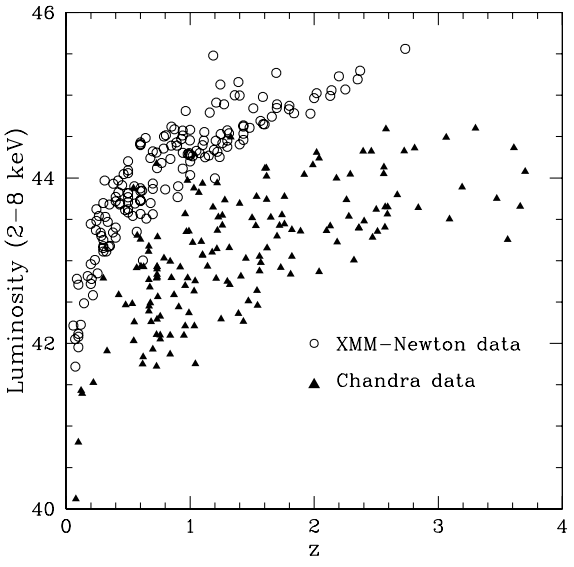

Fig. 3. The 2–8 keV intrinsic luminosity versus redshift plot for the *XMM-Newton* (open circles) and the *Chandra* (filled triangles) sources.

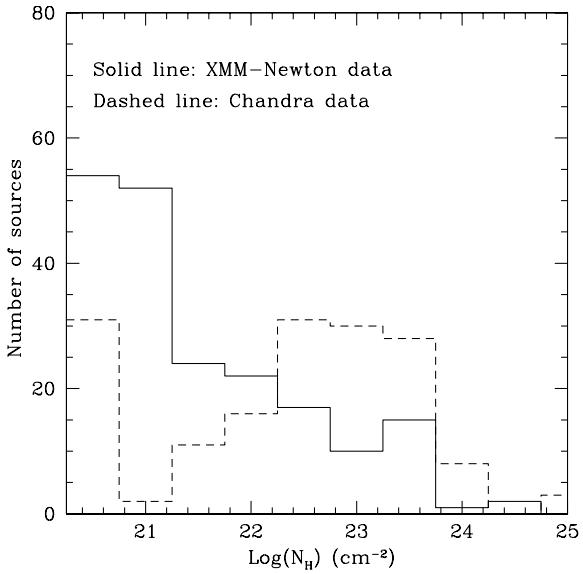

Fig. 4. The $N_{\rm H}$ distribution of the sources in the combined *XMM-Newton* sample (solid line) compared to that derived from the CDF-S observations (dashed line).

4.2. The CDF-S spectral analysis

To cover a much broader flux range, and therefore to examine the widest possible luminosity and redshift range, we also include the data from the CDF-S (Giacconi et al. 2002) in our analysis. In Fig. 3 we plot the intrinsic 2–8 keV luminosity versus redshift for the *Chandra* and the *XMM-Newton* samples. The median luminosity for the *Chandra* dataset is $1.5^{+4.5}_{-1.1} \times 10^{43}$ erg s^{-1}, one order of magnitude lower than that of the *XMM-Newton* data ($2.1^{+3.0}_{-1.5} \times 10^{44}$ erg s^{-1}) due to the significant difference in the flux limit of the observations.

We estimate the $N_{\rm H}$ using X-ray spectral fittings for all 162 CDF-S sources. The spectral files and the auxiliary files were produced from the merged CDF-S event file using the CIAO v.3.2 software, which also corrects the auxillary files for the degradation in the ACIS Quantum Efficiency due to molecular contamination. We consider only the data in the 0.3–8 keV energy range. We adopt a radius of 6 arcsec for the source count extraction and an area 10 times larger for the background estimation. We use the *DMARFADD* task of CIAO to add the ARF files from each observation separately to create a single output file for each source. Similarly, the mean RMF file for each source is extracted using the *ADDRMF* task of *FTOOLS*.

The X-ray spectral fittings are performed using the *XSPEC* v11.2 package. We use the C-statistic technique (Cash 1979). The data are grouped to give a minimum of 1 count per bin to avoid zero count bins. We try to constrain the intrinsic column densities (i.e., subtract the Galactic absorption of 8×10^{19} cm^{-2}, Dickey & Lockman 1990) using an absorbed power-law model with Γ fixed to 1.8.

5. Results

5.1. The N_H distribution

In Fig. 4, we plot the $N_{\rm H}$ distribution for the *XMM-Newton* and *Chandra* samples. The dashed line represents the $N_{\rm H}$ distribution for the 162 sources in the CDF-S survey, and the solid line shows the same distribution for the 171 optically identified sources in the combined *XMM-Newton* sample. The median fluxes are $2.0^{+2.9}_{-0.9} \times 10^{-15}$ erg cm^{-2} s^{-1} and $4.6^{+3.8}_{-1.1} \times 10^{-14}$ erg cm^{-2} s^{-1}, and the median redshifts $1.0^{+0.7}_{-0.3}$ and $0.8^{+0.5}_{-0.4}$ for the *Chandra* and the *XMM-Newton* samples, respectively. When we consider the 26 optically undetected sources at $z = 1.5$, the median redshift for the *XMM-Newton* data becomes $0.9^{+0.5}_{-0.4}$. The errors in the median values correspond to the upper and lower probability quartiles.

Figure 4 demonstrates that there is a large difference between the $N_{\rm H}$ distributions calculated from the *XMM-Newton* and the *Chandra* data. This difference could arise as the *Chandra* sample probes much deeper fluxes. It is well established (e.g., Alexander et al. 2003) that there is a strong correlation between the average hardness ratio and the flux, in the sense that at fainter fluxes we probe harder sources. On the other hand, the *Chandra* observations reveal intrinsically less luminous sources (by approximately an order of magnitude, see Fig. 3). Therefore, it is possible that the difference between the absorption observed in the *XMM-Newton* and *Chandra* samples may also be explained assuming that sources with lower luminosity present, on average, larger amounts of absorption. Next, we will attempt to disentangle these two possibilities.

5.2. N_H-luminosity dependence

We use the data presented above to diagnose whether the strength of the photoelectric absorption depends on the intrinsic luminosity. The simplest way to detect such a possible correlation is to test whether there is a significant decrease in the fraction of obscured objects as the intrinsic luminosity increases. This technique is affected by a selection bias. We observe the unobscured sources within a larger volume compared to the obscured ones, as the observed luminosity of the latter decreases substantially due to photoelectric absorption. To account for this effect, we calculate the fraction of absorbed sources using the $1/V_{\rm m}$ method (see Page & Carrera 2000). For each source of a given observed 2–8 keV luminosity $L_{\rm X}$, we calculate the maximum available volume using the formula:

$$V_{\rm m} = \int_0^{z_{\rm max}} \Omega(f) \frac{{\rm d}V}{{\rm d}z} {\rm d}z,$$

where $\Omega(f)$ is the value of the sensitivity curve at a given flux, corresponding to a source at a redshift z, with observed luminosity L_X and the maximum redshift, z_{max}, at which the source can be observed at the flux limit of the survey. The fraction of the obscured objects at a given luminosity bin is then calculated using the formula:

$$\text{Fraction} = \frac{\sum_{i=1}^{N_1} \frac{1}{V_m(i)}}{\sum_{i=1}^{N} \frac{1}{V_m(i)}},$$

where N_1 is the number of the obscured sources ($N_H > 10^{22}$ cm^{-2}) and N is the total number of the sources in each luminosity bin. The corresponding errors in $1/V_m$ are approximated by:

$$\delta(1/V_m) = \sum_{i=1}^{N_1} \frac{1}{V_m^2(i)},$$

while the errors in the fraction are estimated using the error propagation formula.

We apply this correction in both *XMM-Newton* and *Chandra* observations. The area curve of our *XMM-Newton* survey is constant up to the flux limit of 3×10^{-14} erg cm^{-2} s^{-1} (see Georgakakis et al. 2006a), while the area curve for the CDF-S has been adapted from Giacconi et al. (2002).

In Fig. 5 we plot the estimated fraction of absorbed sources ($N_H > 10^{22}$ cm^{-2}) in a certain luminosity bin as a function of the median luminosity of this bin for the *XMM-Newton* data. When we use only the 171 optically identified sources, there is a marginal reduction in the fraction of obscuration at higher luminosities (>10^{44} erg s^{-1}). This weakens even further when we include the 26 optically faint sources (assuming $z = 1.5$). This is reasonable, since these sources are most probably associated with obscured sources.

In the case of the CDF-S data (Fig. 5), there is again a marginal but constant decrease of the fraction F with increasing luminosity. In a flux limited sample it is reasonable to expect a strong correlation of luminosity with redshift (see Fig. 3). We attempt to break this degeneracy by exploring the fraction of obscured *Chandra* sources as a function of luminosity in a thin redshift slice ($0.7 < z < 1.2$) in Fig. 5. This slice is chosen so as to maximize the number of objects. Finally, in the same panel, we plot the fraction versus luminosity for the high redshift ($z > 1$) *Chandra* sources. The purpose of this is to test whether the fraction of absorbed sources increases at higher redshift. Indeed the K-correction shifts the curvature of the X-ray spectrum caused by the absorption at low energies, i.e., reduces the absorption measured at the observer's frame. This should result in an increased number of absorbed sources at higher redshift. A marginal decrease of F with increasing luminosity exists in all three cases.

However, the small $L - z$ plane coverage of the individual samples does not allow us to provide strong constraints on the $F - L$ dependence. Therefore, to explore the widest luminosity and redshift range we combine the *XMM-Newton* and the *Chandra* datasets. Thus, we obtain a catalogue comprising 359 sources in the 2–8 keV flux range of 6×10^{-16} to 4×10^{-13} erg cm^{-2} s^{-1}. In Fig. 5, we plot the fraction of the obscured sources for the combined (*XMM-Newton* and *Chandra*) sample obtained using the $1/V_m$ method. The combined data reveal a clear decrease in the fraction of absorbed sources at higher luminosities. The best-fit model to the data is also plotted. The fraction of absorbed sources is related to the luminosity according to $F(N_H > 10^{22}\ \text{cm}^{-2}) = 7.075 \times 10^{17} (\text{Log}\, L_X)^{-11.045}$. In the same panel in Fig. 5, we also plot the best-fit models presented in Ueda et al. (2003) and La Franca et al. (2005).

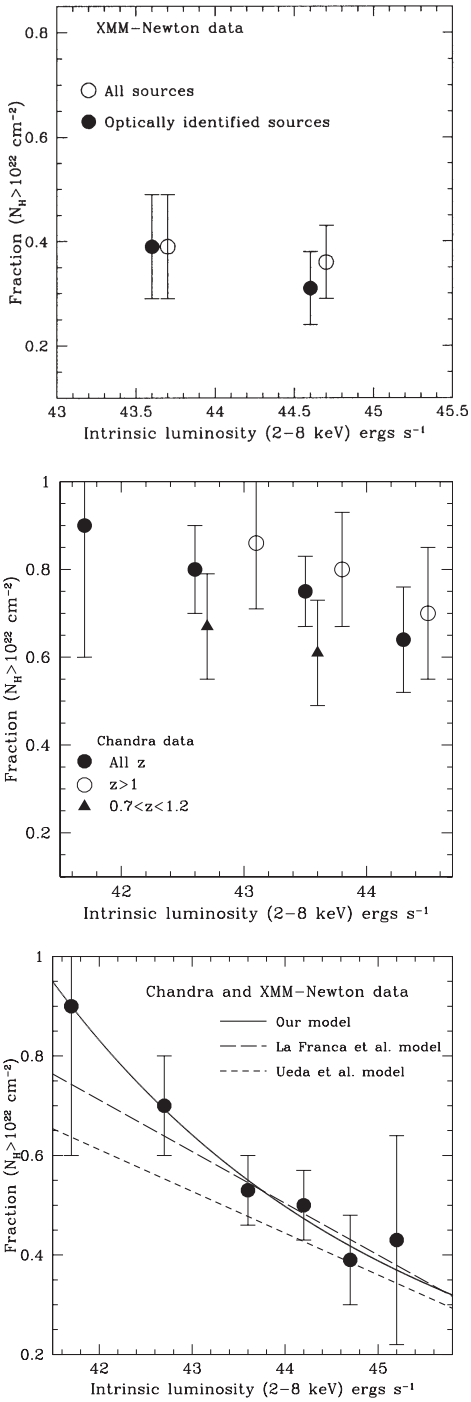

Fig. 5. The fraction of obscured ($N_H > 10^{22}$ cm^{-2}) sources presented in the *XMM-Newton* data (*upper panel*) and the *Chandra* data (*middle panel*), as a function of the 2–8 keV, intrinsic luminosity. In the *lower panel* we plot the same fraction for the combined *XMM-Newton* and *Chandra* samples. In this panel, we also plot our best-fit model and these of Ueda et al. (2003) and La Franca et al. (2005).

In Fig. 6, we plot the fraction F against redshift for the combined *XMM-Newton* and *Chandra* data (the optically unidentified *XMM-Newton* sources are excluded). It is important to note

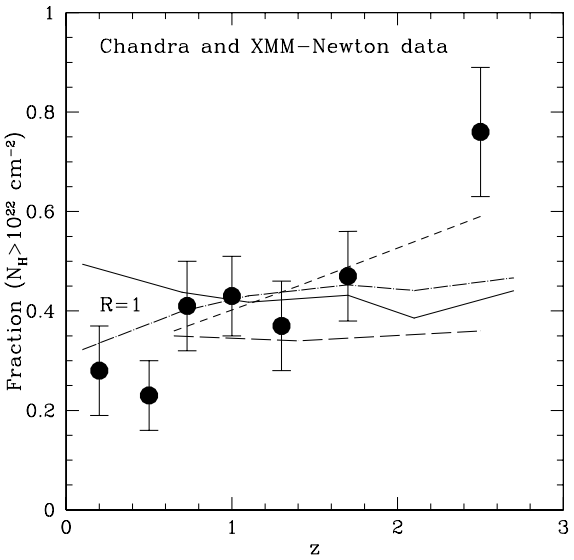

Fig. 6. The *observed* fraction of obscured AGN as a function of redshift. The solid line gives the expected fraction, assuming the luminosity function of Ueda et al. (2003) combined with our best fit model relation between the obscured fraction of AGN and luminosity. The dotted-dashed line gives the expected fraction, assuming no dependence of F on luminosity for a ratio of obscured to unobscured AGN $R = 1$. The long dashed line shows the input distribution of the fraction of obscured sources used in our simulations (see Appendix A), and the short dashed line the resulting one after fitting the simulated spectra.

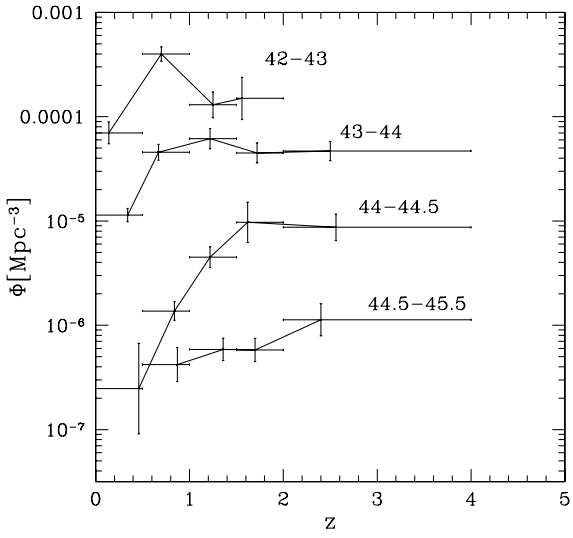

Fig. 7. The space density of the CDF-S AGN as a function of redshift in four luminosity ranges, Log L_X = 42–43, Log L_X = 43–44, Log L_X = 44–44.5, and Log L_X = 44.5–45.5. The errors correspond to the 1σ confidence level.

here that in this plot we are plotting the "observed" fraction as a function of redshift, i.e. we have not applied any $1/V_m$ correction to the data. This allows a direct comparison with the models that predict the expected fraction of sources with redshift for a given survey.

The dashed-dotted line model shows the expected fraction using the Ueda et al. (2003) luminosity function, in the case where there is no dependence of the obscured fraction on luminosity. A value of $R = 1$ for the ratio of obscured to unobscured AGN has been used. Note that the ratio R is related to the fraction F, according to the relation $F = R/(1 + R)$. In this case, the model predictions increase with redshift because of the K-correction, i.e., more obscured sources are detected as the column decreases at higher redshifts according to $(1 + z)^{2.65}$. The solid line model describes the expected fraction of absorbed sources using the luminosity function of Ueda et al. (2003), combined with our best-fit $F - L_X$ relation derived previously. The effect of the steep $F - L_X$ relation is to roughly cancel out the K-correction effect. The data show a significant increase in the fraction of obscured objects, F, at higher redshifts ($z > 2$). This behavior, if not real, may be caused by the photometric redshift estimations, or alternatively, by small fluctuations in the lowest energy bins, which translate to a significant absorption at high z. To test the first possibility, we repeat the calculations considering the photometric and the spectroscopic data separately. The resulting plots are very similar, and there is still an increase of the fraction of obscured sources at high z. Therefore, we conclude that the photometric redshifts cannot introduce this trend. We examine the significance of the second effect by using spectral simulations (see Appendix A for details). In Fig. 6, the input distribution of the obscured sources used in the simulations and the sort dashed line the resulting distribution after fitting the simulated spectra in *XSPEC* are shown. An increase in the fraction F, which is solely introduced by some fluctuations in the lowest energy bins of the spectral files, clearly appears. This suggests that the observed fraction of obscured sources at high z is artificially enhanced. Consequently, there is no significant evidence for an increase in the fraction F with redshift.

Next we investigate the evolution of the AGN space density in different luminosity bins as a function of redshift. For this analysis, we consider only the CDF-S data to use a sample with complete redshift information. The estimation of the space density is based on the $1/V_m$ method. The space densities as a function of redshift are calculated in four luminosity bins in the ranges Log (L_X) 42–43, 43–44, 44–44.5, and 44.5–45.5 erg s^{-1}. The results are plotted in Fig. 7 as a function of the median redshift of each redshift bin. The 1σ errors are also plotted. Figure 7 clearly shows a shift of the number density peak with luminosity in the sense that more luminous AGN peak occurs at an earlier era, while the less luminous ones arise later. There is also evidence for a decline in the density of the lower luminosity QSOs (Log L_X < 44 erg s^{-1}), and especially those at 42 < Log L_X < 43. This trend is known as cosmic downsizing, and it has previously been reported by Ueda et al. (2003), Fiore et al. (2003), and Barger et al. (2005). Hasinger et al. (2005) also found similar results, analyzing the space density of type-I QSOs.

6. Discussion

In this paper, we use the largest *XMM-Newton* sample with X-ray spectroscopic information available to investigate the behavior of intrinsic absorption in AGN as a function of redshift and luminosity. We also take advantage of the complete optical coverage (photometric or spectroscopic) of the CDF-S observations to extend our results at fainter fluxes (down to $\sim 6 \times 10^{-16}$ erg cm^{-2} s^{-1}).

In Fig. 5, we plot the fraction of obscured objects as a function of luminosity separately for the *XMM-Newton*, the *Chandra* data and their combination. Despite the weak indications of a decline of this fraction in the individual samples, the only way to unambiguously verify this correlation is to increase the coverage of the $L - z$ plane by combining the two samples. It is likely that the rapid decline appearing in the combined sample could not be easily observed in the *XMM-Newton* and the

Table 3. The median values for the 2–8 keV observed flux for each luminosity bin in the combined sample.

Log L_X[1]	f_X[2]
42.7	1.7×10^{-15}
43.6	5.3×10^{-15}
44.5	3.1×10^{-14}
45.2	5.6×10^{-14}

[1] Logarithm of the median value of 2–8 keV in units of erg s^{-1}. [2] Median value of the 2–8 keV observed flux in units of erg cm^{-2} s^{-1}.

Chandra individual datasets, due to the limited available volume of each independent, flux limited survey. For example, *Chandra* does not cover a large enough volume to sample a large number of luminous sources. However, we caution that the combination of these different subsamples may introduce some bias in favor of an $F - L_X$ correlation. Indeed, as we move toward higher luminosities, we sample more *XMM-Newton* sources and fewer *Chandra* sources in each luminosity bin, according to Fig. 3. However the *XMM-Newton* sources are found in much brighter fluxes in comparison with the *Chandra* ones. Thus, as we move progressively to higher luminosities, we sample higher fluxes and hence less obscured sources, according to the well known flux-absorption correlation. This effect is summarized in Table 3 where we list the median 2–8 keV flux for each luminosity bin presented in Fig. 5.

The decrease of the fraction of obscured sources as a function of luminosity is consistent with the results of La Franca et al. (2005). The physical interpretation of this model could be that the radiation pressure flattens the torus in luminous objects (Königl & Kartje 1994) or increases the degree of photoionization of the gas around them. Another possible scenario is that of the "receding torus", which has been proposed by Lawrence (1991) and has been recently updated by Simpson (2005), where, because of the effects of dust sublimation, the inner radius of the torus increases with luminosity.

One way to explore whether the relation between the absorbed fraction and luminosity ($F - L_X$ relation) is real (or is induced to some degree by the strong flux-absorption correlation), is to model the number of absorbed sources as a function of flux. In Fig. 8 we plot the fraction of obscured AGN as a function of the flux. We plot the *XMM-Newton* points, the CDF-S points, as well those from the *Chandra* survey in the Extended Groth Strip (Georgakakis et al. 2006b) separately, and compare them with various model predictions. In the above models, we use the Ueda et al. (2003) luminosity function. The solid line gives the predictions of our model and uses the $F - L_X$ relation derived here. The long dashed line corresponds to a model with a ratio of obscured to unobscured AGN, $R = 4$ (or $F = 0.8$) with no dependence on luminosity. This is the ratio derived in the local universe by Risaliti et al. (1999) and Maiolino & Rieke (1995). The short dashed line corresponds to the $R = 1$ case with no dependence on luminosity. The $R = 1$ model nicely represents the *XMM-Newton* data while the $R = 4$ model follows the faint CDF-S data better. However, only a model that includes a decrease in the $F - L_X$ relation can explain the abrupt increase of the fraction of absorbed sources with decreasing flux.

Previous estimates are in agreement with our results. Piconceli et al. (2003), analyzing hard X-ray *XMM-Newton* data, claimed that the observed fraction of obscured sources at bright fluxes ($>10^{-13}$ erg cm^{-2} s^{-1}) is about 30 per cent, much lower than that predicted by the ($R = 4$) XRB model.

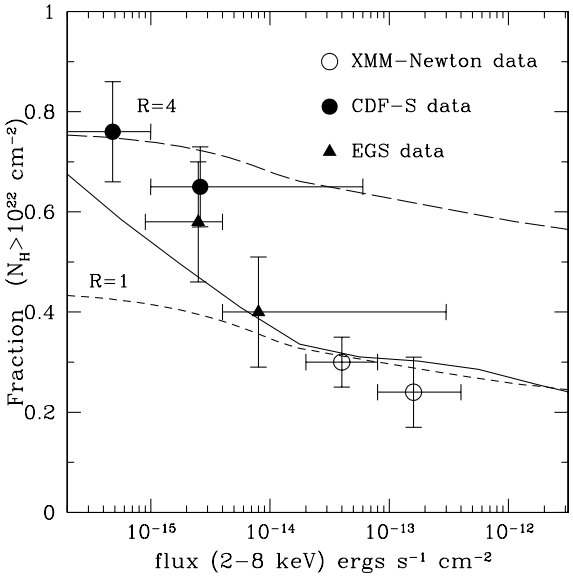

Fig. 8. The fraction of the sources with $N_H > 10^{22}$ cm^{-2} for the *XMM-Newton* sample (open circles) and the *Chandra* sample (filled circles). The triangles represent the EGS *Chandra* survey of Georgakakis et al. (2006b). The solid line gives the predicted fraction using the $F - L_X$ relation derived here. The long and short dashed lines give the models with $R = 4$ and $R = 1$ ratios of obscured to unobscured AGN, respectively, with no dependence on luminosity.

La Franca et al. (2005), combining data from different X-ray samples, studied the behavior of obscuration in a much wider flux range. Their findings for the fraction of obscured sources are very similar to ours in both faint and bright fluxes. Their proposed $F-L_X$ relation is in agreement with our model (see Fig. 5). Note that here we have used a power-law best-fit model instead of a linear one.

Figure 6 shows the dependence of F on redshift. The fraction shows an apparent increase with redshift, with a more abrupt increase at high redshifts, $z > 2$. Ueda et al. (2003) find no dependence of the fraction F on redshift. Ballantyne et al. (2006) propose that the obscuration may be related to star formation within the host galaxy, and thus there may be some increase of the obscured AGN fraction with redshift. They test their models by comparing with the observed type-I AGN in the CDF-N (Barger et al. 2003). These authors find an obscured fraction F evolving as $(1 + z)^{0.3}$, together with a dependence of F on luminosity. La Franca et al. (2005) find a dependence on redshift very similar to ours (see their Fig. 6, right panel): the fraction F increases from ∼0.2 at low redshift to $F \sim 0.6$ at $z > 2$. In our case, however, our simulations show that the lowest energy bins fluctuations can introduce a significant artificial correlation of the fraction F with redshift. This effect becomes particularly important at high redshifts due to the K-correction effect. This suggests that the observed fraction of obscured sources at high z is erroneously enhanced. Consequently, there is no significant evidence for an increase in the fraction F with redshift.

7. Summary

We have combined bright *XMM-Newton* (from SDSS fields and the XMM1dF survey) and faint *Chandra* (from CDF-S) data to form the largest sample (359 sources in the 2–8 keV band) with X-ray spectra. Our goal is to investigate the intrinsic AGN obscuring column density as a function of luminosity and redshift.

This bears important implications on AGN unification models, as well as the X-ray background population synthesis models. The CDF-S has complete redshift coverage ensuring that there is no bias because of optically unidentified sources at faint fluxes. At bright fluxes, the level of redshift incompleteness is less than 15 per cent. We use the $1/V_{\rm m}$ method to estimate the fraction, F, of obscured to unobscured AGN. This properly takes into account the bias introduced by the fact that obscured sources are fainter in flux, and thus are preferentially detected in smaller numbers and at preferentially lower redshifts. Our findings can be summarized as follows:

The fraction of obscured AGN, F decreases with increasing luminosity. This confirms previous results by Ueda et al. (2003) and La Franca et al. (2005). The dependence of the fraction F on luminosity naturally reproduces the observation that the number of obscured sources increases drastically with decreasing flux.

There is tentative evidence for a increase of the fraction F with increasing redshift. However, this is mainly based on the high redshift bins ($z > 2$), and thus should be viewed with caution. Our simulations show that these bins are affected by systematic overestimates of the column density, caused by small fluctuations in the lowest energy spectral bins.

Acknowledgements. We thank the referee Dr. A. Comastri for the valuable comments and suggestions. This work has been supported by the program Promotion of Excellence in Research, grant "X-ray Astrophysics with ESA's mission XMM" funded jointly by the European Union and the Greek Ministry of Development. This work is based on data obtained from the *XMM-Newton* and CXC public data archives. We acknowledge the use of data from the Sloan Digital Sky Survey.

References

Alexander, D. M., Bauer, F. E., Brandt, W. N., et al. 2003, AJ, 126, 539
Ballantyne, D. R., Everett, J. E., & Murray, N. 2006, ApJ, 639, 740
Barger, A. J., Cowie, L. L., Capak, P., et al. 2003, AJ, 126, 632
Barger, A. J., Cowie, L. L., Mushotzky, R. F., et al. 2005, AJ, 129, 578
Cash, W. 1979, ApJ, 228, 939
Coleman, G. D., Wu, C., & Weedman, D. W. 1980, ApJS, 43, 393
Comastri, A., Setti, G., Zamorani, G., & Hasinger, G. 1995, A&A, 296, 1
Dickey, J. M., & Lockman, F. J. 1990, AR&A, 28, 215
Downes, A. J. B., Peacock, J. A., Savage, A., & Carrie, D. R. 1986, MNRAS, 218, 31
Fiore, F., Brusa, M., Cocchia, F., et al. 2003, A&A, 409, 79
Georgakakis, A., Georgantopoulos, I., Stewart, G. C., Shanks, T., & Boyle B. J. 2003, MNRAS, 344, 161
Georgakakis, A., Georgantopoulos, I., Vallbe, M., et al. 2004, MNRAS, 349, 135
Georgakakis, A., Georgantopoulos, I., & Akylas, A. 2006a, MNRAS, 366, 171
Georgakakis, A., Nandra, K., Laird, E. S., et al. 2006b, MNRAS, 371, 221
Georgantopoulos, I., & Georgakakis, A. 2005, MNRAS, 358, 131
Georgantopoulos, I., Georgakakis, A., Akylas, A., et al. 2004, MNRAS, 352, 91
Giacconi, R., Zirm, A., Wang, J., et al. 2002, ApJS, 139, 369
Gilli, R., Salvati, M., & Hasinger, G. 2001, A&A, 366, 407
Hatziminaoglou, E., Mathez, G., & Pelló, R. 2000, A&A, 359, 9
Hasinger, G., Miyaji, T., & Schmidt, M. 2005, A&A, 441, 417
Kitsionas, S., Hatziminaoglou, E., Georgakakis, A., & Georgantopoulos, I. 2005, A&A, 434, 475
Königl, A., & Kartje, J. F. 1994, ApJ, 434, 446
La Franca, F., Fiore, F., Comastri, A., et al. 2005, ApJ, 635, 864
Lawrence, A. 1991, MNRAS, 252, 586
Maiolino, R., & Rieke, G. H. 1995, ApJ, 454, 95
Mushotzky, R. F., Cowie, L. L., Barger, A. J., & Arnaud, K. A. 2000, Nature, 404, 459
Norman, C., Ptak, A., Hornschemeier, A., et al. 2004, ApJ, 607, 721
Page, M. J., & Carrera, F. J. 2000, MNRAS, 311, 433
Perola, G. C., Puccetti, S., Fiore, F., et al. 2004, A&A, 421, 491
Piconcelli, E., Cappi, M., Bassani, L., et al. 2002, A&A, 394, 835
Risaliti, G., Maiolino, R., & Salvati, M. 1999, ApJ, 522, 157
Simpson, C. 2005, MNRAS, 360, 565
Stocke, J. T., Morris, S. L., Gioal, I. M., et al. 1991, ApJS, 76, 813
Stoughton, C., Adelman, J., & Annis, J. T. 2002, SPIE, 4836, 339
Szokoly, G. P., Bergeron, J., & Hasinger, G. 2004, ApJS, 155, 271
Treister, E., Urry, C. M., Chatzichristou, E., et al. 2004, ApJ, 616, 123
Ueda, Y., Akiyama, M., Ohta, K., & Miyaji, T. 2003, ApJ, 598, 886
Zheng, W., Mikles, V. J., Mainieri, V., et al. 2004, ApJS, 155, 73

Online Material

Table 2. The X-ray spectral fitting results for the 153 sources of our *XMM-Newton*/SDSS sample.

No.	RA (J2000)	Dec (J2000)	Γ^1	$N_{\rm H_{obs}}^2$	$F_{2-8\ \rm keV}^3$	z	$N_{\rm H_{gal}}^4$	$N_{\rm H_{intr}}^5$	Log $(L_{2-8\ \rm keV})^6$	ID^7
1	10.696	1.005	$2.56^{+0.54}_{-0.40}$	<0.06	2.18	1.00	2.32	0.06	44.03	2
2	10.710	1.035	$2.77^{+0.28}_{-0.23}$	<0.05	2.43	0.60	2.34	0.03	43.56	2
3	10.802	0.934	$1.93^{+0.13}_{-0.11}$	<0.02	7.60	0.94	2.32	0.06	44.51	2
4	10.908	0.770	$1.85^{+0.31}_{-0.25}$	<0.05	3.50	2.13	2.31	0.21	44.99	2
5	10.921	0.881	$1.68^{+0.36}_{-0.29}$	$0.25^{+0.16}_{-0.12}$	5.54	4.40	2.32	20.10	45.87	2
6	10.922	0.935	$1.92^{+0.12}_{-0.10}$	<0.02	8.71	0.94	2.32	0.06	44.57	2
7	10.959	0.963	$2.10^{+0.2}_{-0.16}$	$0.14^{+0.05}_{-0.04}$	17.8	0.10	2.34	0.15	42.71	2
8	11.056	0.861	$2.31^{+0.44}_{-0.32}$	<0.06	4.66	0.94	2.34	0.06	44.30	1
9	28.011	1.079	1.80	<0.02	3.83	1.05	2.80	0.07	44.32	2
10	28.020	1.134	1.80	$0.30^{+0.18}_{-0.14}$	4.21	0.40	2.80	0.68	43.40	2
11	28.126	0.950	1.80	$0.07^{+0.02}_{-0.03}$	3.31	0.35	2.80	0.11	43.17	2
12	28.159	1.156	1.80	$1.08^{+0.77}_{-0.38}$	4.19	0.10	2.79	1.36	42.08	2
13	28.179	1.205	1.80	$0.50^{+1.08}_{-0.36}$	2.36	1.40	2.79	4.88	44.41	2
14	28.190	1.184	1.80	<0.06	1.59	1.51	2.79	0.11	44.30	2
15	28.244	1.085	$2.59^{+0.55}_{-0.36}$	<0.10	1.78	0.65	2.80	0.04	43.50	1
16	28.280	1.098	$1.65^{+0.35}_{-0.33}$	<0.075	7.16	0.20	2.80	0.01	42.95	2
17	29.820	0.504	$2.10^{+0.67}_{-0.38}$	<0.12	10.8	0.35	2.60	0.02	43.67	2
18	29.990	0.553	$2.09^{+0.16}_{-0.15}$	<0.02	26.9	0.31	2.62	0.02	43.96	1
19	30.105	0.488	1.80	<0.41	4.82	0.30	2.60	0.02	43.18	2
20	30.120	0.480	$2.34^{+0.67}_{-0.28}$	<0.06	6.87	0.17	2.60	0.02	42.81	1
21	40.090	–8.361	1.80	< 0.02	4.15	1.30	3.11	0.09	44.57	2
22	40.106	–8.408	$2.15^{+0.17}_{-0.18}$	$0.15^{+0.05}_{-0.05}$	31.3	–	3.12	1.42	45.59	3
23	40.169	–8.295	1.80	$0.15^{+0.22}_{-0.12}$	2.16	–	3.09	1.47	44.43	3
24	40.327	–8.428	1.80	<0.04	3.69	1.43	3.09	0.10	44.62	2
25	44.025	0.276	1.80	<0.02	4.95	0.60	6.50	0.03	43.87	2
26	44.113	0.126	1.80	<0.09	3.48	0.34	6.50	0.44	43.17	2
27	44.158	0.234	1.80	$2.05^{+1.12}_{-1.25}$	4.11	–	6.52	23.01	44.71	3
28	44.188	0.008	1.80	<0.05	6.59	0.50	6.51	0.07	43.81	2
29	44.211	0.226	1.80	<0.032	3.79	1.00	6.66	1.88	44.27	2
30	45.518	0.274	$1.80^{+0.15}_{-0.22}$	$0.04^{+0.05}_{-0.04}$	5.24	4.28	7.17	1.97	45.82	2
31	45.527	–0.022	$1.88^{+0.11}_{-0.09}$	$0.07^{+0.02}_{-0.02}$	17.1	0.64	7.15	0.19	44.48	1
32	45.563	–0.059	1.80	$0.35^{+0.07}_{-0.08}$	2.32	4.53	7.15	30.67	45.52	2
33	45.780	0.171	$2.17^{+0.15}_{-0.13}$	$0.07^{+0.02}_{-0.03}$	3.53	1.02	7.08	0.36	44.26	2
34	54.475	0.493	1.80	<0.04	4.26	2.02	8.22	0.19	45.02	2
35	54.542	0.390	$2.35^{+0.54}_{-0.39}$	<0.15	2.74	1.12	8.12	0.18	44.25	1
36	54.562	0.490	$2.20^{+0.20}_{-0.25}$	<0.2	9.13	–	8.21	0.11	45.06	3
37	54.577	0.198	1.80	<0.05	3.11	1.58	7.92	0.12	44.65	1
38	54.616	0.420	1.80	$0.06^{+0.02}_{-0.03}$	2.61	1.30	8.15	0.36	44.37	2
39	54.656	0.346	1.80	$2.80^{+4.20}_{-1.60}$	3.40	0.70	8.10	11.33	43.86	2
40	54.677	0.357	1.80	$0.09^{+0.04}_{-0.04}$	2.44	1.52	8.11	0.81	44.48	2
41	59.203	1.359	$2.20^{+0.55}_{-0.38}$	$0.36^{+0.18}_{-0.14}$	7.13	–	13.3	3.85	44.95	3
42	59.243	1.349	1.80	$0.09^{+0.06}_{-0.05}$	3.22	–	13.3	0.84	44.60	3
43	59.282	1.260	$2.35^{+0.29}_{-0.33}$	$0.27^{+0.18}_{-0.13}$	3.00	–	13.2	2.83	44.58	3
44	59.322	1.295	$1.85^{+0.16}_{-0.14}$	<0.04	5.87	–	13.3	0.11	44.87	3
45	59.480	1.239	$1.61^{+0.53}_{-0.38}$	<0.22	5.42	1.51	13.3	0.74	44.84	2
46	127.611	52.694	$2.04^{+0.09}_{-0.11}$	$0.09^{+0.02}_{-0.03}$	5.86	–	3.96	0.73	44.87	3
47	127.611	52.767	$1.89^{+0.15}_{-0.15}$	$0.06^{+0.04}_{-0.04}$	4.57	0.60	3.96	0.15	43.83	2
48	127.707	52.819	$1.76^{+0.10}_{-0.09}$	$0.03^{+0.02}_{-0.02}$	9.19	1.40	3.89	0.10	44.99	2
49	127.785	52.644	$1.86^{+0.14}_{-0.17}$	$0.38^{+0.16}_{-0.11}$	4.13	0.20	3.87	0.58	42.72	2
50	127.821	52.588	$0.25^{+0.45}_{-0.25}$	>500	6.87	–	3.85	500	44.93	3

Table 2. continued.

No.	RA(J2000)	Dec(2000)	Γ^1	$N_{\rm H_{obs}}^2$	$F_{2-8\ \rm keV}^3$	z	$N_{\rm H_{gal}}^4$	$N_{\rm H_{intr}}^5$	$L_{2-8\ \rm keV}^6$	ID[7]
51	127.822	52.815	$1.81^{+0.07}_{-0.11}$	<0.05	3.96	0.70	3.87	0.05	43.93	2
52	127.912	52.701	1.80	$18.33^{+2.17}_{-3.13}$	17.0	0.05	3.84	21.30	42.21	1
53	128.020	52.922	1.80	$3.30^{+0.67}_{-0.88}$	5.76	0.99	3.84	20.53	44.45	2
54	128.076	52.623	$2.05^{+0.12}_{-0.17}$	<0.07	2.63	1.22	3.79	0.08	44.31	2
55	139.188	51.695	$1.72^{+0.17}_{-0.14}$	<0.026	12.4	0.50	1.47	0.03	44.09	2
56	139.516	51.687	1.80	$0.16^{+0.03}_{-0.05}$	3.13	0.10	1.45	0.18	41.95	2
57	139.821	51.691	1.80	$0.33^{+0.47}_{-0.22}$	2.46	0.80	1.41	1.47	43.86	2
58	143.417	55.111	$2.64^{+0.56}_{-0.29}$	<0.08	1.50	0.90	1.89	0.05	43.76	2
59	143.450	55.312	$1.65^{+0.08}_{-0.09}$	$0.10^{+0.03}_{-0.02}$	17.7	0.60	1.89	0.28	44.42	2
60	143.497	55.263	$1.82^{+0.11}_{-0.16}$	<0.05	4.60	1.70	1.88	0.14	44.88	2
61	143.650	61.270	$1.60^{+0.36}_{-0.25}$	<0.02	3.89	1.90	2.69	0.15	44.87	2
62	143.744	61.209	$1.25^{+0.55}_{-0.4}$	$1.40^{+1.22}_{-1.10}$	15.2	0.25	2.65	2.47	43.48	1
63	143.889	61.461	1.80	$2.14^{+0.32}_{-0.60}$	4.56	0.47	2.72	5.95	43.61	1
64	143.898	61.322	$2.46^{+0.21}_{-0.14}$	$0.04^{+0.03}_{-0.02}$	3.85	0.50	2.67	0.05	43.58	2
65	144.030	61.546	$2.62^{+0.28}_{-0.32}$	$0.16^{+0.06}_{-0.09}$	2.50	–	2.76	1.54	44.50	3
66	144.035	61.507	$1.78^{+0.41}_{-0.23}$	<0.072	3.52	0.60	2.73	0.03	43.72	2
67	144.266	61.266	1.80	$0.29^{+0.68}_{-0.20}$	0.72	–	2.51	3.06	43.95	3
68	144.270	61.440	$2.17^{+0.54}_{-0.37}$	<0.06	2.55	1.43	2.57	0.38	44.46	2
69	144.373	61.432	1.80	$1.74^{+1.03}_{-0.71}$	3.62	–	2.56	19.50	44.66	3
70	187.651	64.425	1.80	<0.05	3.47	0.60	2.05	0.03	43.72	2
71	187.793	64.313	1.80	$0.04^{+0.01}_{-0.02}$	3.58	0.60	2.00	0.06	43.73	2
72	188.077	64.052	$1.89^{+0.25}_{-0.27}$	$0.05^{+0.06}_{-0.05}$	5.64	2.20	1.94	0.61	45.22	2
73	191.103	–0.410	$1.73^{+0.09}_{-0.07}$	<0.02	8.75	0.40	1.76	0.02	43.71	2
74	191.122	–0.571	$1.66^{+0.52}_{-0.37}$	$0.38^{+0.36}_{-0.26}$	7.70	1.01	1.77	2.26	44.58	2
75	191.124	–0.413	$1.44^{+0.27}_{-0.48}$	$0.17^{+0.19}_{-0.15}$	5.45	–	1.76	1.70	44.83	3
76	191.170	–0.420	$1.95^{+0.14}_{-0.16}$	$0.19^{+0.04}_{-0.06}$	4.38	–	1.75	1.92	44.74	3
77	191.224	–0.356	$1.92^{+0.09}_{-0.12}$	$0.08^{+0.03}_{-0.03}$	4.01	1.10	1.74	0.44	44.39	2
78	191.240	–0.271	$1.93^{+0.27}_{-0.19}$	<1.83	3.98	0.12	1.73	0.07	42.22	1
79	191.250	–0.355	$1.82^{+0.15}_{-0.05}$	<0.04	3.09	1.30	1.74	0.09	44.45	2
80	191.317	–0.316	$1.88^{+0.06}_{-0.09}$	<0.03	6.61	1.58	1.73	0.12	44.97	1
81	191.421	–0.463	$1.80^{+0.05}_{-0.07}$	$0.03^{+0.02}_{-0.02}$	11.1	1.69	1.73	0.18	45.27	1
82	191.490	–0.510	$1.66^{+0.26}_{-0.17}$	<0.05	3.18	0.40	1.73	0.02	43.27	2
83	195.740	67.501	$1.98^{+0.31}_{-0.19}$	<0.04	3.01	1.84	1.85	0.16	44.78	1
84	195.903	67.507	$1.63^{+0.36}_{-0.17}$	<0.06	15.9	0.30	1.85	0.02	43.69	2
85	195.996	67.509	$0.75^{+0.46}_{-0.31}$	<0.02	11.5	0.50	1.85	500	44.05	2
86	196.225	67.501	$2.38^{+0.16}_{-0.12}$	<0.02	2.93	0.54	1.85	0.03	43.54	1
87	196.459	67.655	$1.63^{+0.26}_{-0.17}$	<0.07	16.0	0.50	1.85	0.03	44.20	2
88	205.150	–0.446	1.80	$3.88^{+8.78}_{-3.04}$	4.81	–	1.93	43.76	44.78	3
88	205.161	0.321	$2.64^{+0.74}_{-0.54}$	<0.20	4.22	0.50	1.84	0.32	43.62	2
90	205.188	–0.400	1.80	$0.46^{+0.30}_{-0.18}$	5.12	0.50	1.91	1.29	43.70	2
91	205.209	0.265	1.80	$0.48^{+0.18}_{-0.39}$	4.15	–	1.84	5.21	44.72	3
92	205.325	–0.389	$1.70^{+0.30}_{-0.20}$	<0.02	9.81	0.42	1.93	0.03	43.82	1
93	205.339	–0.230	1.80	<0.02	5.43	0.73	1.87	0.04	44.11	1
94	205.363	0.237	1.80	<0.02	4.18	1.69	1.85	0.14	44.84	1
95	205.368	–0.522	1.80	$1.78^{+0.22}_{-0.61}$	16.4	0.60	2.01	6.12	44.39	2
96	205.418	0.262	1.80	$0.05^{+0.05}_{-0.03}$	3.23	0.25	1.85	0.06	42.84	1
97	205.428	0.210	$1.79^{+0.06}_{-0.06}$	<0.03	11.0	0.79	1.85	0.05	44.54	1
98	205.487	0.502	1.80	<0.02	2.19	1.23	1.86	0.08	44.25	1
99	205.550	0.497	1.80	$0.19^{+0.38}_{-0.16}$	1.66	0.57	1.86	0.56	43.35	1
100	205.643	0.539	1.80	<22	3.80	2.01	1.87	0.18	44.96	2
101	205.678	0.539	1.80	<0.07	4.15	–	1.88	0.62	44.72	3
102	205.692	–0.595	1.80	<0.04	7.92	0.79	2.10	0.05	44.35	1
103	205.731	0.110	1.80	<0.02	6.68	0.44	1.89	0.03	43.69	1

Table 2. continued.

No.	RA(J2000)	Dec(J2000)	Γ^1	$N_{\rm H_{obs}}^2$	$F_{2-8\ \rm keV}^3$	z	$N_{\rm H_{gal}}^4$	$N_{\rm H_{intr}}^5$	$L_{2-8\ \rm keV}^6$	ID[7]
104	205.735	0.015	$1.93^{+0.62}_{-0.4}$	$0.03^{+0.26}_{-0.03}$	10.9	0.80	1.91	0.07	44.51	1
105	205.756	0.442	1.80	$0.06^{+0.03}_{-0.03}$	5.13	1.51	1.89	0.45	44.81	2
106	205.849	0.205	1.80	<0.02	10.6	0.87	1.90	0.05	44.58	1
107	205.871	0.026	1.80	<0.15	4.46	2.35	1.94	0.25	45.19	1
108	205.881	0.413	1.80	<0.24	1.30	1.20	1.90	0.08	43.99	2
109	205.886	–0.034	1.80	<0.13	3.02	1.60	1.96	0.12	44.64	1
110	205.928	0.300	1.80	$0.15^{+0.16}_{-0.09}$	5.63	1.11	1.91	0.95	44.55	1
111	205.948	0.339	1.80	<0.04	12.3	0.24	1.91	0.02	43.36	1
112	205.949	–0.033	1.80	$0.39^{+0.94}_{-0.39}$	2.66	–	1.97	4.19	44.52	3
113	205.963	0.077	1.80	<0.02	7.45	0.07	1.95	0.01	42.05	1
114	205.968	–0.075	1.80	$1.13^{+0.67}_{-0.67}$	9.73	–	1.99	12.58	45.09	3
115	206.083	0.071	1.80	$0.35^{+0.15}_{-0.15}$	5.72	0.30	1.97	0.66	43.25	2
116	206.083	–0.519	1.80	<0.02	2.42	0.68	2.15	0.04	43.69	1
117	206.092	–0.572	1.80	$0.27^{+0.10}_{-0.07}$	2.45	0.22	2.17	0.42	42.58	1
118	206.102	–0.218	1.80	<0.03	4.48	1.11	2.06	0.07	44.45	1
119	206.105	–0.307	1.80	$0.16^{+0.10}_{-0.10}$	2.55	1.97	2.09	2.51	44.77	1
120	206.151	0.556	1.80	<0.02	3.02	1.43	1.94	0.10	44.53	1
121	206.161	–0.183	1.80	$2.82^{+3.51}_{-1.70}$	8.03	–	2.07	31.74	45.00	3
122	206.212	0.279	1.80	$0.12^{+0.03}_{-0.07}$	3.82	1.43	1.97	1.05	44.63	2
123	206.220	0.089	$2.34^{+0.11}_{-0.11}$	<0.02	28.0	0.08	2.02	0.01	42.78	1
124	206.241	–0.600	1.80	$11.60^{+18.40}_{-4.60}$	13.2	0.46	2.21	31.86	44.04	1
125	206.243	0.272	1.80	<0.03	4.82	0.15	1.98	0.01	42.48	1
126	206.248	–0.266	$1.90^{+0.41}_{-0.34}$	<0.02	21.1	0.24	2.12	0.02	43.62	1
127	206.283	–0.091	1.80	<0.02	8.51	0.73	2.09	0.04	44.30	1
128	206.290	0.347	1.80	$0.27^{+0.19}_{-0.13}$	5.89	0.50	1.98	0.73	43.76	2
129	207.012	60.109	1.80	$2.38^{+2.50}_{-1.43}$	2.67	–	1.82	26.75	44.52	3
130	207.248	60.250	$1.95^{+0.17}_{-0.11}$	<0.03	6.61	0.50	1.81	0.03	43.81	2
131	207.367	60.104	$1.89^{+0.26}_{-0.15}$	<0.06	4.53	0.10	1.80	0.01	42.11	2
132	207.492	60.330	1.80	$1.64^{+1.70}_{-0.34}$	5.91	–	1.80	18.34	44.87	3
133	235.760	54.153	1.80	$0.03^{+0.03}_{-0.01}$	4.38	0.61	1.25	0.04	43.84	2
134	235.967	54.001	$2.35^{+0.25}_{-0.17}$	$0.03^{+0.04}_{-0.02}$	3.30	1.48	1.25	0.13	44.60	2
135	235.998	53.984	$2.30^{+0.14}_{-0.11}$	$0.12^{+0.05}_{-0.05}$	5.57	2.37	1.25	2.50	45.29	1
136	236.007	54.127	1.80	<0.02	2.24	-	1.24	0.11	44.45	3
137	236.101	53.929	$1.49^{+0.40}_{-0.17}$	<0.10	9.68	0.70	1.25	0.04	44.32	2
138	236.147	54.094	$1.95^{+0.47}_{-0.32}$	<0.07	3.19	1.00	1.24	0.06	44.19	2
139	255.174	64.216	$1.84^{+0.76}_{-0.3}$	<0.25	21.8	0.20	2.67	0.02	43.44	2
140	255.196	64.384	1.80	$2.20^{+3.50}_{-1.12}$	16.9	0.60	2.69	7.57	44.40	2
141	255.252	64.202	$1.96^{+0.54}_{-0.3}$	<0.25	7.49	2.73	2.66	0.33	45.56	1
142	255.349	64.236	$2.12^{+0.53}_{-0.36}$	<0.16	10.2	0.45	2.65	0.06	43.91	1
143	354.221	0.347	1.80	<0.06	3.02	0.94	3.85	0.06	44.11	2
144	354.312	0.376	1.80	$2.52^{+2.48}_{-1.18}$	4.40	–	3.83	28.34	44.74	3
145	354.382	0.433	1.80	<0.03	4.14	0.30	3.82	0.02	43.11	2
146	354.408	0.268	1.80	$2.60^{+0.38}_{-0.52}$	9.89	0.40	3.82	6.29	43.77	2
147	354.547	0.345	$1.82^{+0.23}_{-0.19}$	<0.045	8.15	0.28	3.79	0.02	43.33	1
148	354.582	0.186	1.80	$0.70^{+0.30}_{-0.25}$	5.37	–	3.80	7.70	44.83	3
149	354.630	0.356	1.80	<0.48	0.62	0.62	3.78	0.04	43.00	2
150	358.456	–10.523	1.80	<0.03	1.68	0.70	2.92	0.04	43.56	2
151	358.466	–10.257	1.80	$0.21^{+0.07}_{-0.07}$	4.56	0.30	2.86	0.38	43.15	2
152	358.540	–10.359	$1.71^{+0.16}_{-0.13}$	<0.03	6.40	0.55	2.88	0.03	43.89	2
153	358.643	–10.268	$1.53^{+0.22}_{-0.23}$	$0.05^{+0.11}_{-0.05}$	9.89	1.36	2.87	0.30	44.99	2

[1] When the photon index is fixed to 1.8 the spectral fittings are performed using the C-statistic technique. [2] Observed, best fit $N_{\rm H}$ value in units of 10^{22} cm^{-2}. [3] Intrinsic 2–8 keV flux in units of 10^{-14} erg cm^{-2} s^{-1}. [4] Galactic column density in the directions of the observed field in units of 10^{20} cm^{-2}. [5] Intrinsic rest frame column density in units of 10^{22} cm^{-2}. [6] Logarithm of intrinsic 2–8 keV luminosity in units of erg s^{-1}. [7] The ID values (ID = 1, 2 or 3) indicate spectroscopic, photometric or the absence of an optical counterpart respectively.

Appendix A: Validity of the N_H estimations: spectral simulations

We describe here the strategy we followed to check the validity of the derived $N_{\rm H}$ estimations through the spectral analysis. Given that a small fluctuation in the lowest energy bin in our *Chandra* spectral files might correspond to an apparently high absorption at high z, we tried some simulations to quantify this effect. First we constructed 920 fake spectral files with exactly the same redshift and flux distribution suggested from the SDF-S data. Each spectral file presents an arbitrary amount of absorption in the range of 10^{20}–10^{23} cm^{-2} and a photon index of 1.8. These fake files are fitted in XSPEC to obtain a value for the observed column density. The obtained values are converted to the intrinsic $N_{\rm H}$ value based on the formula $N_{\rm Hintr} = (N_{\rm Hobs} - N_{\rm Hgal}) \cdot (1 + z)^{2.65}$. The results are plotted in Fig. A.1. The solid line histogram describes the initial $N_{\rm H}$ distribution of all the sources, and the short dashed line the corresponding one, after fitting the fake data in XSPEC. Also, the dotted line histogram shows the initial distribution of the low redshift ($z < 1$) sources, and the short dashed line the resulting $N_{\rm H}$ distribution for the same population. Clearly, the spectral fitting analysis produces a significant increase in the number of obscured ($N_{\rm H} > 10^{22}$ cm^{-2}) sources in comparison to the initial distribution. The same plot suggests that this effect is almost negligible in the low z population. Our conclusion is that high z sources suffer from a systematic increase in the measured column density. This overestimate is about 50 per cent at $z \sim 2.5$, 20 per cent at $z \sim 1.5$, and becomes almost negligible at $z < 1$.

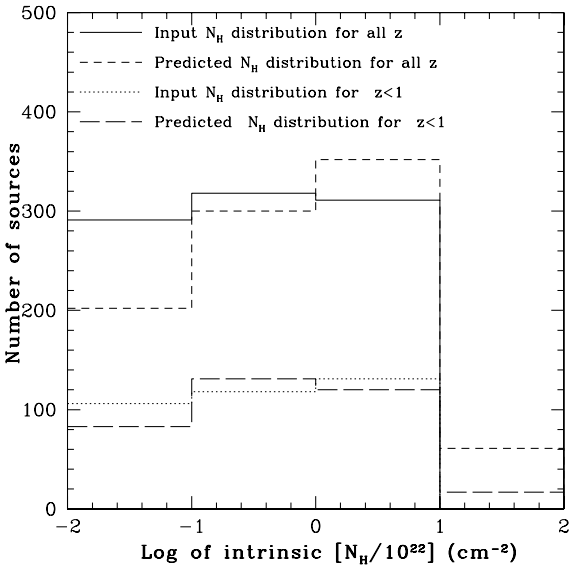

Fig. A.1. This plot summarizes the results of the performed simulations concerning the validity of the spectral analysis of the CDF-S data. The solid line histogram describes the initial $N_{\rm H}$ distribution of all sources, and the short dashed line the corresponding one, after fitting the faked data in XSPEC. Similarly, the dotted and the long dashed histograms show the same results, using only the low z ($z < 1$) data.